PEER REVIEWED

Comparison of Microstructures and Selected Properties of Plasma-Sprayed Iron-Based Metallic Glass Coatings

Aleksandra Małachowska[1] · Paweł Sokołowski[1] · Gerd Paczkowski[2] ·
Thomas Lampke[2] · Adam Sajbura[1]

Abstract The three powders $(Fe_{0.9}Co_{0.1})_{76-}Mo_4(P_{0.45}C_{0.2}B_{0.2}Si_{0.15})_{20}$, $Fe_{48}Mo_{14}Cr_{15}Y_2C_{15}B_6$, and $Fe_{56.04}Co_{13.45}Nb_{5.5}B_{25}$ were produced by gas atomization and sieved to the fraction of + 15 to 50 μm. The chemical compositions of the powders were selected to cover three groups of iron-based metallic glass alloys, which were separated in terms of non-metal elements: B, C, and P included in these alloys. The powder morphology and size distribution were determined. The coatings were then prepared on steel substrates with atmospheric plasma spraying. The coating microstructures were characterized by light microscopy, scanning electron microscopy, and their phase compositions were confirmed by XRD. Additionally, the hardness and Young's moduli were studied with nanoindentation. The bond strength of the coatings was determined by a pull-off test. Finally, the wear properties were evaluated with the rubber wheel test according to the ASTM G65-04 standard. For the $Fe_{48}Mo_{14}Cr_{15}Y_2C_{15}B_6$ coatings, it was possible to preserve the fully amorphous structure, and these coatings were characterized by the lowest wear loss values.

Keywords amorphous structure · atmospheric plasma spraying · coatings · iron-based metallic glasses · wear resistance

✉ Aleksandra Małachowska
aleksandra.malachowska@pwr.edu.pl

1 Wroclaw University of Technology, ul. Lukasiewicza 5, 50-371 Wroclaw, Poland

2 Institute of Materials Science and Engineering, Chemnitz University of Technology, Erfenschlager Straße 73, 09125 Chemnitz, Germany

Introduction

Iron-based metallic glasses are seen as a good candidate for wear/corrosion resistant coatings (Ref 1). Due to the small thickness of the coatings (up to several hundred micrometers), it is possible to achieve sufficient cooling rates and preserve an amorphous structure, which is one of the main issues limiting the processing and application of metallic glasses. The iron-based metallic glasses proved to have superior wear and corrosion resistance prevailing, e.g., the HVOF sprayed SS316L coatings (Ref 2). The corrosion resistance of metallic glasses is excellent mainly due to the alloying elements and the homogeneous structure (Ref 3). They usually contain Cr, Mo, and P. Cr is regarded as the element that provides the highest passivation ability of the Fe-based metallic glasses (Ref 4). Mo enhances the Cr influence since it prevents the dissolution of Cr during passivation (Ref 5). Additionally, metallic glasses demonstrate the structurally and chemically homogeneous single-phase nature and lack of crystalline defects, including the grain boundary. Therefore, the passivation film is uniform (Ref 3).

The wear of material is usually inversely proportional to its hardness (Ref 6). It is also reported that the presence of nanocrystals improves the strength and toughness of the

material and hence wear resistance (Ref [7, 8]). Several thermal spraying methods have already been tested for the deposition of metallic glass coatings, including high-velocity oxygen fuel (HVOF) (Ref [9]), atmospheric plasma spraying (APS) (Ref [10]), or cold gas dynamic spraying (CGDS) (Ref [11]). Thermal spraying techniques are an effective way to prepare various high-quality coatings without influencing the substrate material. The key feature is the possibility of controlling and limiting the temperature during the spraying of metallic glass in the range close to the glass transition temperature (Ref [9]). APS is getting more and more attention in this field because it is more convenient and economical than other thermal spray technologies such as HVOF, low-pressure plasma spraying (LPPS), and vacuum plasma spraying (VPS) (Ref [12]). The typical cooling rates of a single particle can achieve 10^7 to 10^8 K/s (Ref [13]) during spraying, which is sufficient for vitrification. However, the processing of metallic glasses by APS also has some limitations. The content of the amorphous phase varies with plasma spray parameters but is usually lower than that of the initial feedstock material (Ref [12]). This is the result of heat accumulation during subsequent spray passes. Moreover, the powder oxidizes during atmospheric plasma spraying, facilitating the formation of crystallites. The APS sprayed coatings have a mostly dense layered structure with pores and micro-cracks originating from the loosely packed structure, gas porosity, and shrinkage. The main wear mechanisms in the case of plasma-sprayed coating include brittle fracture and splat detachment. Plasma-sprayed coatings are prone to detachment of the splats, and unfortunately, the low toughness of metallic glasses favors brittle fracture during the friction processes (Ref [12, 14]). Consequently, the correlation to the microhardness is not linear but depends on inter-splat binding (arc power), crystallite amount, and their size in the coatings (Ref [5]).

Iron-based metallic glasses might be classified into three main groups FeC(B), FeB, and FeP(C), based on metalloid glass-forming elements that differ in glass-forming ability, strength, hardness, and ductility. The FeC(B) and FeB-type glasses show high strength and hardness but much lower ductility than FeP(C) type (Ref [15]). Usually, FeC(B) types are processed because of their high glass-forming ability. The usually deposited alloys include: $Fe_{41.87}Cr_{14.37}Ni_{1.06}Mo_{11.33}C_{20.82}B_{7.15}Si_{3.40}$ (Ref [16]), $Fe_{45}Cr_{16}Mo_{16}C_{18}B_5$ (Ref [17]), $Fe_{48}Cr_{15}Mo_{14}C_{15}B_6Y_2$ (Ref [18, 19]), $Fe_{73}Cr_2Si_{11}B_{11}C_3$ (Ref [20–22]), $FeSi_{3.1}B_{4.5}$ (Ref [23]). In particular, the $Fe_{48}Cr_{15}Mo_{14}Y_2C_{15}B_6$ alloy is widely studied (Ref [1, 10, 24]) because of its excellent corrosion resistance and relatively high glass-forming ability (Ref [24]). In present study, $Fe_{48}Mo_{14}Cr_{15}Y_2C_{15}B_6$ was compared to two other alloys $(Fe_{0.9}Co_{0.1})_{76}Mo_4(P_{0.45}C_{0.2}B_{0.2}Si_{0.15})_{20}$ and $Fe_{56.04}Co_{13.45}Nb_{5.5}B_{25}$. The $(Fe_{0.9}Co_{0.1})_{76}Mo_4(P_{0.45}C_{0.2}B_{0.2}Si_{0.15})_{20}$ alloy is characterized by enhanced plasticity while continuing to exhibit good mechanical properties and a high tendency to vitrification (Ref [25]). The alloys from Fe-Co-Nb-B systems exhibit an ultrahigh compressive strength reaching 4.5 GPa (Ref [26]). The selection of these three alloys allows the cover of three groups of iron-based metallic glasses, namely FeC(B), FeB, and FeP(C).

Materials and Methods

Feedstock Characterization

Three types of metallic glass powder were selected for coatings: (1) $Fe_{48}Mo_{14}Cr_{15}Y_2C_{15}B_6$, (2) $(Fe_{0.9}Co_{0.1})_{76}Mo_4(P_{0.45}C_{0.2}B_{0.2}Si_{0.15})_{20}$, (3) $Fe_{56.04}Co_{13.45}Nb_{5.5}B_{25}$. The powders were custom made (Nannowal GmbH & Co. KG, Berlin, Germany) by gas atomization and then sieved to the desired fraction + 15 to 50 μm. The size distributions of the powders were analyzed by wet laser diffraction (HELOS/BR, Sympatec GmbH) and are within the assumed range. SEM images of the powders used and their size distribution are shown in Fig.[1]. Two powders ($(Fe_{0.9}Co_{0.1})_{76}Mo_4(P_{0.45}C_{0.2}B_{0.2}Si_{0.15})_{20}$ and $Fe_{56.04}Co_{13.45}Nb_{5.5}B_{25}$ are mostly spherical, while the third powder $Fe_{48}Mo_{14}Cr_{15}Y_2C_{15}B_6$ is partially elongated and irregular in shape. A similar shape of these powder particles was observed by Manai (Ref [27]). The precipitations are visible in the selected particles of the $Fe_{56.04}Co_{13.45}Nb_{5.5}B_{25}$ powder (Fig. [1]g). These may be the α-FeCo precipitations observed during the crystallization of alloys from the Fe-Co-Nb-B group (Ref [28]). However, since no clear peaks were observed in XRD (Fig. [4]), they were not accurately identified. All three powders show a slight porosity within the particles. During gas atomization, the so-called bag break-up may occur. A melt fragment is shaped into a bag-like form that spreads in the gas flow direction. The bag may then shatter into fine droplets or close, forming a large drop (hollow sphere) with a trapped atomization gas inside (Ref [29]). Apart from gas velocity, the formation of hollow spheres is directly related to the viscosity of the melt. The higher the viscosity, the greater the possibility of gas trapping (Ref [30]). The metallic glasses exhibit large viscosity; therefore, gas porosity inside the iron-based metallic powder particles is likely to occur.

Thermal Spray

The deposition of coatings was performed using an atmospheric plasma spraying process.

The process was carried out by one cathode-one anode SG-100 plasma torch (Praxair), which was installed on a 6-axis industrial robot. In order to limit the heat input
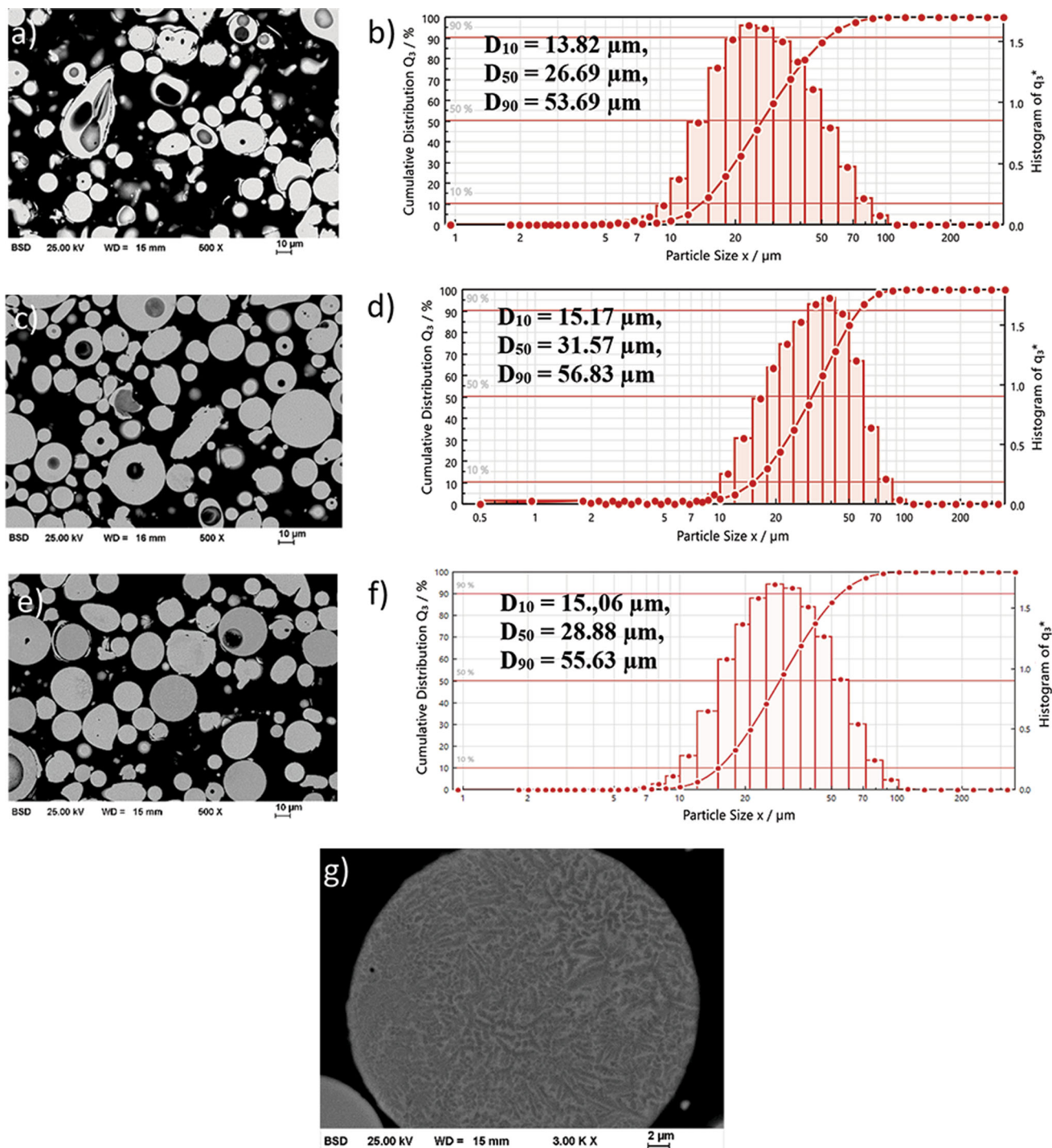
Fig. 1 Cross sections and size distributions of used powders: (a, b) $Fe_{48}Mo_{14}Cr_{15}Y_2C_{15}B_6$, (c, d) $(Fe_{0.9}Co_{0.1})_{76}Mo_4(P_{0.45}C_{0.2}B_{0.2}Si_{0.15})_{20}$, (e–g) $Fe_{56.04}Co_{13.45}Nb_{5.5}B_{25}$

during spraying, the plasma was formed by using pure argon only, with a flow rate equal to 45 slpm. Electric power was also limited to a constant value equal to 22 kW. The powder was injected radially and externally into a plasma jet. The powder feed rate was set as a 20 g min^{-1}, which was controlled during the deposition process. Argon was used as a carrier gas with a flow rate of 3 slpm.

On the contrary, the substrates were mounted on a carousel and rotated by a turntable. The rotational speed was set to ensure the relative velocity between the plasma torch
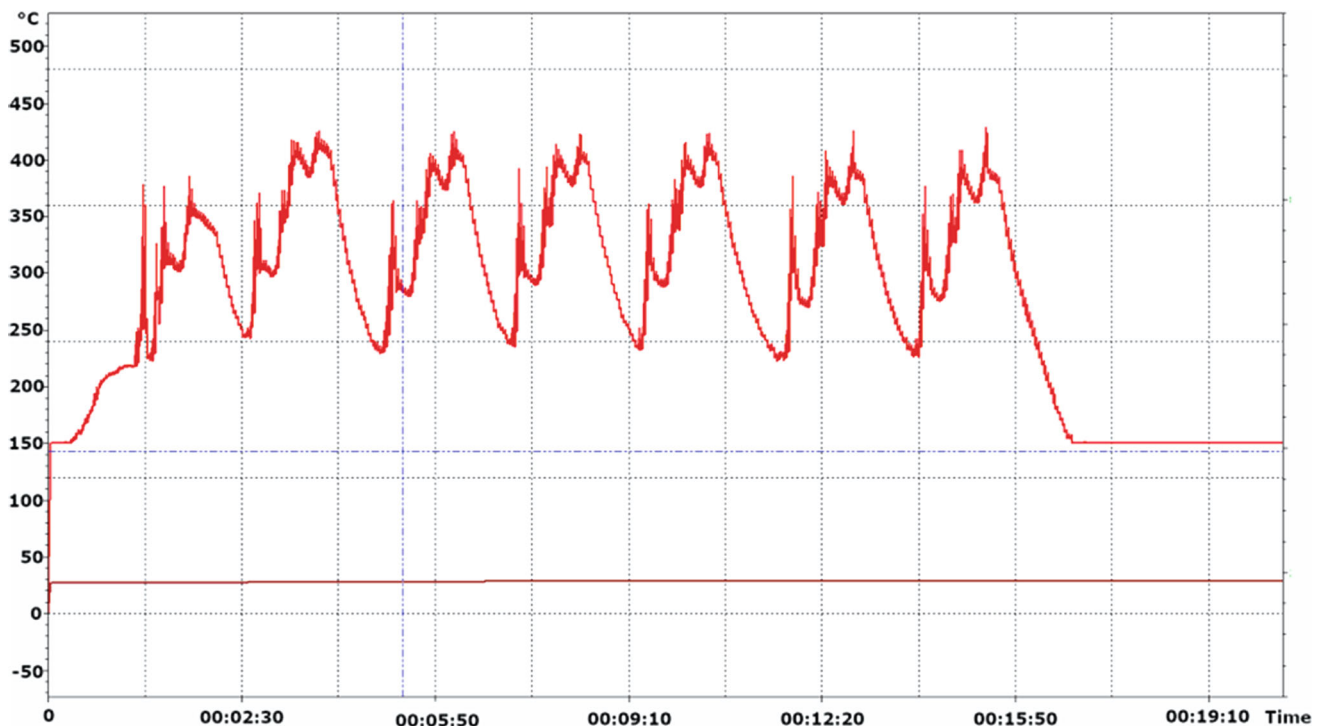
Fig. 2 The representative plasma spray thermal history recorded by infrared pyrometer

and the substrates as 400 mm s^{-1}. The spray stand-off distance was set to be 90 mm. The substrates used in this work were made of S235 steel and were in the form of coupons 40 mm in diameter and 10 mm in thickness. The substrates were sand-blasted and cleaned with ethanol directly before plasma spray deposition. The described spray procedure was similar for each type of powder feedstock.

An infrared pyrometer monitored the thermal history on the face side of the samples to keep the narrow regime of temperature changes (as shown in Fig. 2). The substrates were preheated before spraying to ∼ 200 °C, and then the spray cycles were programmed so that they did not exceed ∼ 450 °C. The samples were also intensively cooled by air-blades during spraying.

Coatings Characterization

Metallographic specimens were prepared from the deposited coatings and then subjected to observation with a digital light microscope (LM, Keyence VHX-6000) and scanning electron microscopes equipped with EDS (SEM, Tescan Vega 3, and ZEISS LEO1455VP). Based on the micrographs, porosity and coating thicknesses were calculated using ImageJ software. X-ray diffraction was performed on the samples to identify the phases present in the coatings. XRD measurements (Rigaku Ultima IV Diffractometer) were performed with Cu Kα irradiation (λ =

1.5406 Å) in the range of angles 2θ from 20° to 90°, a step of 0.05 and an exposure time of 4 s per point. Nanoindentation (Anton Paar, NHT3) was performed with a Berkovich-type tip, calibrated on fused silica samples. The applied load was set to 50 mN and the dwell time to 30 s. The loading and unloading rates were equal to 100 mN/min. The hardness and elastic modulus were calculated using the Oliver and Pharr method (Ref 31). At least ten measurements were taken for each coating, and an average was calculated. Furthermore, Vickers microhardness was measured under a 2.49 N load. Similarly, at least ten indentations were made, and the average value was calculated. The bond strength was determined by a pull-off test carried out with an Elcometer 510 tester (Elcometer Instruments, Manchester, UK). Epoxy adhesive Distal Classic (Libella, Warsaw, Poland) was used to bond a counterpart with a diameter of 10 mm to the coating. The pin was pulled with a constant pressure rate of 0.4 MPa/s. After the test, the failure mode was determined. The average value and standard deviation were calculated based on three measurements. To investigate the wear characteristics of the samples, a rubber wheel wear test was carried out according to ASTM: G-65-04 (Ref 32) standard with a load of 130 N and a sliding distance of 71.8 m (0.5 min), 718 m (5 min), and 1436 m (10 min). The three specimens of each coating were tested, and an average value was reported. The samples were weighed before and after the wear test with a high accuracy balance.
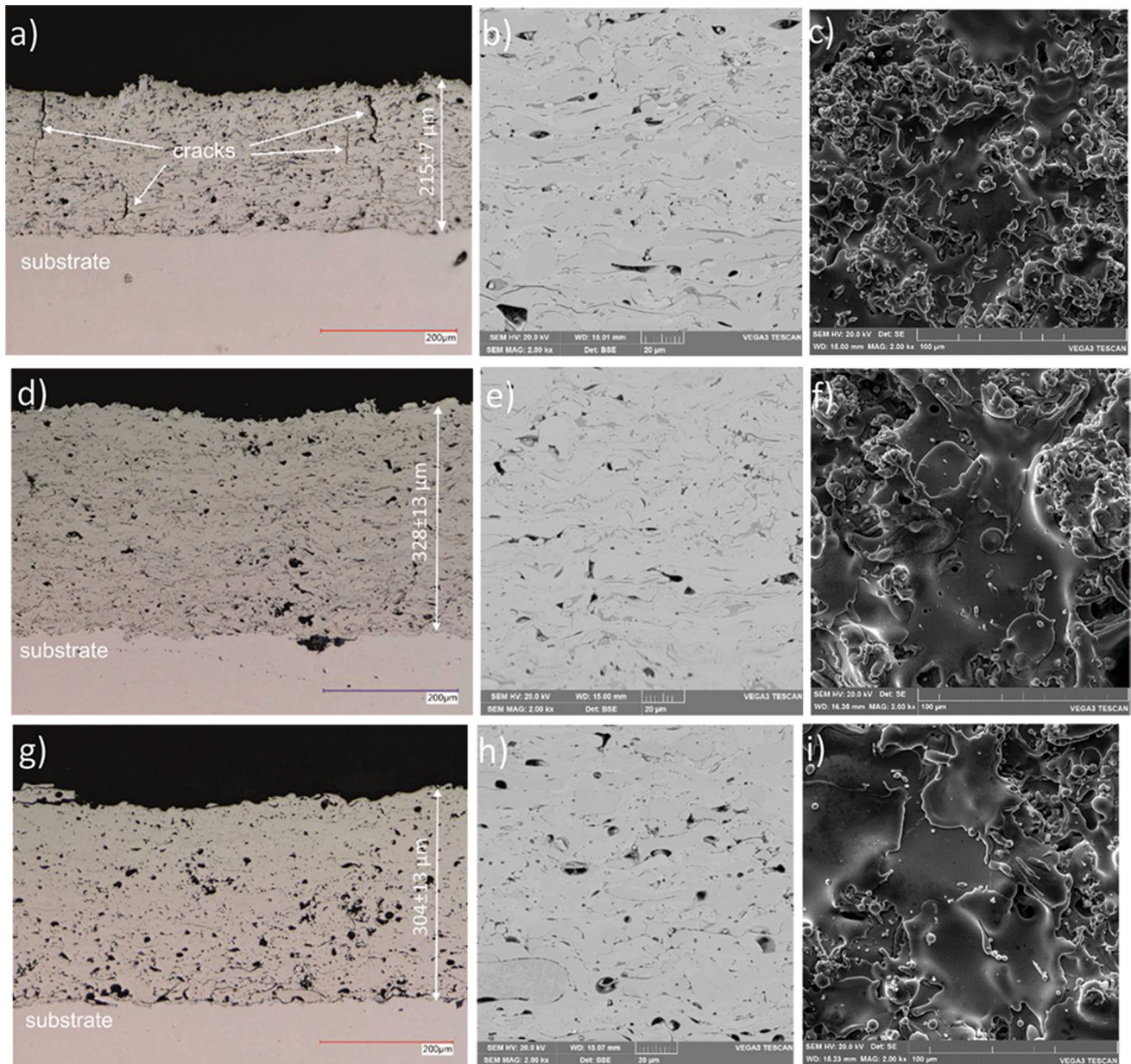
Fig. 3 Cross sections of the deposited coatings: (a–c) $Fe_{48}Mo_{14}Cr_{15}Y_2C_{15}B_6$, (d–f) $(Fe_{0.9}Co_{0.1})_{76}Mo_4(P_{0.45}C_{0.2}B_{0.2}Si_{0.15})_{20}$, (g–i) $Fe_{56.04}Co_{13.45}Nb_{5.5}B_{25}$

Discussion and Results

Microstructure

The low and high magnification micrographs of the deposited coatings are shown in Fig. 3 for both cross section and surface. All coatings have a typical lamellar microstructure and good adhesion to the substrate. The $Fe_{48}Mo_{14}Cr_{15}Y_2$-$C_{15}B_6$ coating has the lowest thickness of ~ 215 μm. This is due to the elongated shape of the powder particles, which caused them to block in the powder feeder and thus hindered their uniform feeding. The thickness of the other two coatings is comparable ~ 328 μm for $(Fe_{0.9}Co_{0.1})_{76}$-$Mo_4(P_{0.45}C_{0.2}B_{0.2}Si_{0.15})_{20}$ and ~ 308 μm for $Fe_{56.04}$-$Co_{13.45}Nb_{5.5}B_{25}$. Oxidation is very limited in the $Fe_{56.04}Co_{13.45}Nb_{5.5}B_{25}$ coating, contrary to the rest of the coatings. The highest porosity of $\sim 5.3\%$ was recorded for the $Fe_{56.04}Co_{13.45}Nb_{5.5}B_{25}$ coating. The pores are visible as dark regions and partially aggregated, forming single clusters. The $Fe_{48}Mo_{14}Cr_{15}Y_2C_{15}B_6$ and $(Fe_{0.9}Co_{0.1})_{76}$-$Mo_4(P_{0.45}C_{0.2}B_{0.2}Si_{0.15})_{20}$ coatings exhibit lower porosity of ~ 3.7 and $\sim 2.8\%$, respectively. Additionally, the diameter of the pores is, on average lower than for $Fe_{56.04}Co_{13.45}$-$Nb_{5.5}B_{25}$. Furthermore, randomly distributed vertical micro-

cracks and cracks are visible in the $Fe_{48}Mo_{14}Cr_{15}Y_2C_{15}B_6$ coating. These cracks run through the entire coating or occur near the substrate or at the top of the coating. A similar phenomenon was also mentioned by Xie et al. (Ref 33). Numerous cracks in the $Fe_{48}Mo_{14}Cr_{15}Y_2C_{15}B_6$ coating could be attributed, among other factors, to the shape of the powder. Powder feeding was not perfectly stable during the deposition process, which caused differences in the thermal history of various particles. This, in turn, led to an increase in thermal stresses and finally to crack formation. Iron-based metallic glasses are brittle materials, and therefore, it is not possible to reduce the resulting thermal stresses through plastic deformation. The two remaining coatings ($Fe_{0.9}Co_{0.1})_{76}Mo_4(P_{0.45}C_{0.2}B_{0.2}Si_{0.15})_{20}$ and $Fe_{56.04}Co_{13.45}Nb_{5.5}B_{25}$ were free of cracks. The surface of all coatings was also observed. In the case of the $Fe_{48}Mo_{14}Cr_{15}Y_2C_{15}B_6$ coating, the surface consists of well-melted splats, but the fine, partially, or even non-melted particles are visible in the coating structure. This was probably caused by the fraction of fine particles observed in this powder feedstock, as $Fe_{48}Mo_{14}Cr_{15}Y_2C_{15}B_6$ had the lowest d10. These fine powders were not perfectly injected into the core of the plasma jet and traveled in colder plasma periphery regions. Thus, they were not perfectly heated by the plasma jet. The other two coatings, that is, $(Fe_{0.9}Co_{0.1})_{76}Mo_4(P_{0.45}C_{0.2}B_{0.2}Si_{0.15})_{20}$, and $Fe_{56.04}Co_{13.45}Nb_{5.5}B_{25}$, showed a much more uniform surface. The splats are homogenously flattened and cover most of the surface, with just a single very fine non-melted powder particle embedded in the coating structure.

The chemical composition of the deposited coatings (Table 1) agrees with the target chemical composition. All elements are included besides boron. Boron is a light element and cannot be measured accurately with a standard EDS detector. Therefore, it was omitted. The carbon content is clearly overestimated, but its measurement using an EDS cannot be considered fully reliable.

X-ray Diffraction

XRD patterns are shown in Fig. 4. In all coatings, a halo peak appears, which confirms that an amorphous phase is present. It is most evident in the case of $Fe_{48}Mo_{14}Cr_{15}Y_2C_{15}B_6$. The glass-forming ability (GFA) of $Fe_{56.04}Co_{13.45}Nb_{5.5}B_{25}$

seems to be lower than $Fe_{48}Mo_{14}Cr_{15}Y_2C_{15}B_6$, which is evidenced by a smaller halo peak in the XRD pattern. The $Fe_{48}Mo_{14}Cr_{15}Y_2C_{15}B_6$ material is known for its exceptional glass-forming ability (Ref 24). Additionally, crystallization peaks are present in $(Fe_{0.9}Co_{0.1})_{76}Mo_4(P_{0.45}C_{0.2}B_{0.2}Si_{0.15})_{20}$ coating, which were not present in the feedstock powder. Other peaks coming, e.g., from oxides, were not detected, which indicates their low content. Heating the metallic glass above crystallization reduces the free volume and consequently causes embrittlement of metallic glass (Ref 34, 35). However, there is a particular critical volume of crystallites above which the ductility of the metallic glasses increases (Ref 36). The increase in coating toughness after crystallization was observed exemplary by Yasir et al. (Ref 37).

Bond Strength

The bond strength of the coatings was investigated by a pull-off test. The results are presented in Fig. 5. The lowest bond strength of 30.1 MPa was observed for $Fe_{48}Mo_{14}Cr_{15}Y_2C_{15}B_6$. The bond strength of $(Fe_{0.9}Co_{0.1})_{76}Mo_4(P_{0.45}C_{0.2}B_{0.2}Si_{0.15})_{20}$ and $Fe_{56.04}Co_{13.45}Nb_{5.5}B_{25}$ was comparable and amounted to $\sim$ 40 MPa. The fracture type was adhesive in all cases. Usually, the tiny fragment of the coating was ripped off, as shown in Fig. 5. The observed bond strength values are similar to the 25–41 MPa reported by Peng et al. (Ref 38) for HVOF sprayed $Fe_{48}Mo_{14}Cr_{15}Y_2C_{15}B_6$ coatings and much higher than 14.9–18.9 MPa reported by Wang et al. (Ref 39) for plasma-sprayed Fe-based coatings on Al-Si substrate. Although the adhesion of metallic glass coatings can reach up to > 68 MPa when applied with HVOF (Ref 40) the obtained values are high enough not to cause increased abrasive wear. Especially, since there was an adhesive type of fracture.

Nanoindentation and Microhardness Measurements

The values obtained from the indentation test and microhardness measurement are shown in Table 2. The difference between the Vickers test values and the recalculated hardness value from the nanoindentation test is approximately $\sim$ 200 HV. The highest one might be noticed for $Fe_{56.04}Co_{13.45}Nb_{5.5}B_{25}$. The differences are caused by

Table 1. Chemical composition of deposited coatings

Coating	Fe at.%	Cr at.%	Mo at.%	Y at.%	Co at.%	Nb at.%	C at.%	P at.%	Si at.%
$Fe_{48}Mo_{14}Cr_{15}Y_2C_{15}B_6$	44,26	12,63	15,05	1,35	…	…	26,71	…	…
$(Fe_{0.9}Co_{0.1})_{76}Mo_4(P_{0.45}C_{0.2}B_{0.2}Si_{0.15})_{20}$	61,90	…	3,59	…	8,36	…	16,72	7,56	1,87
$Fe_{56.04}Co_{13.45}Nb_{5.5}B_{25}$	72,90	…	…	…	20,76	6,33	…	…	…

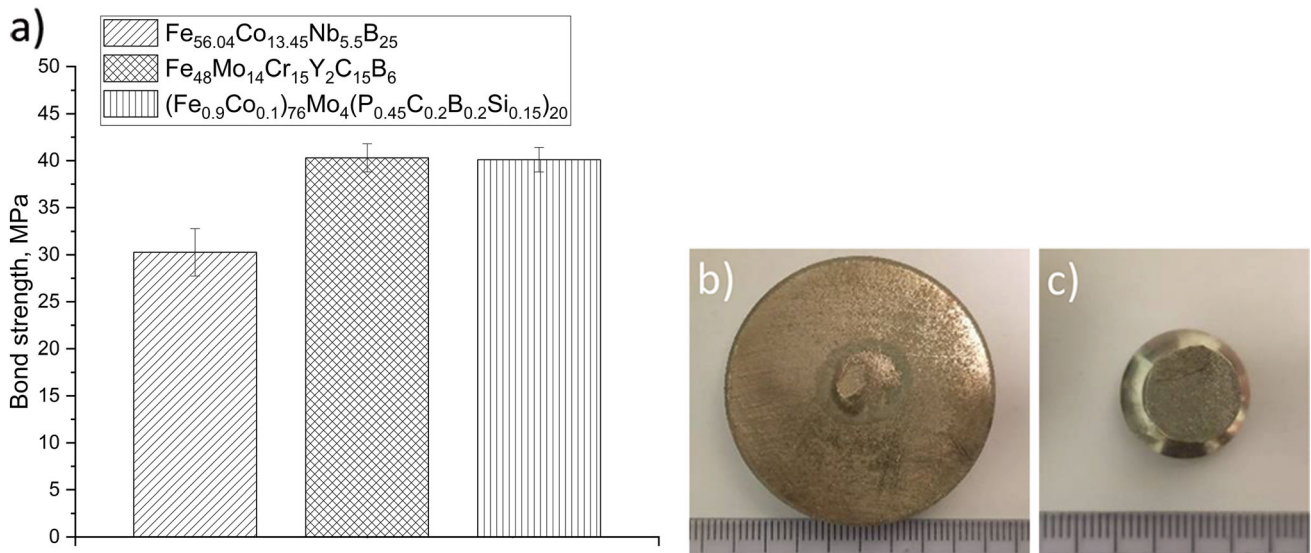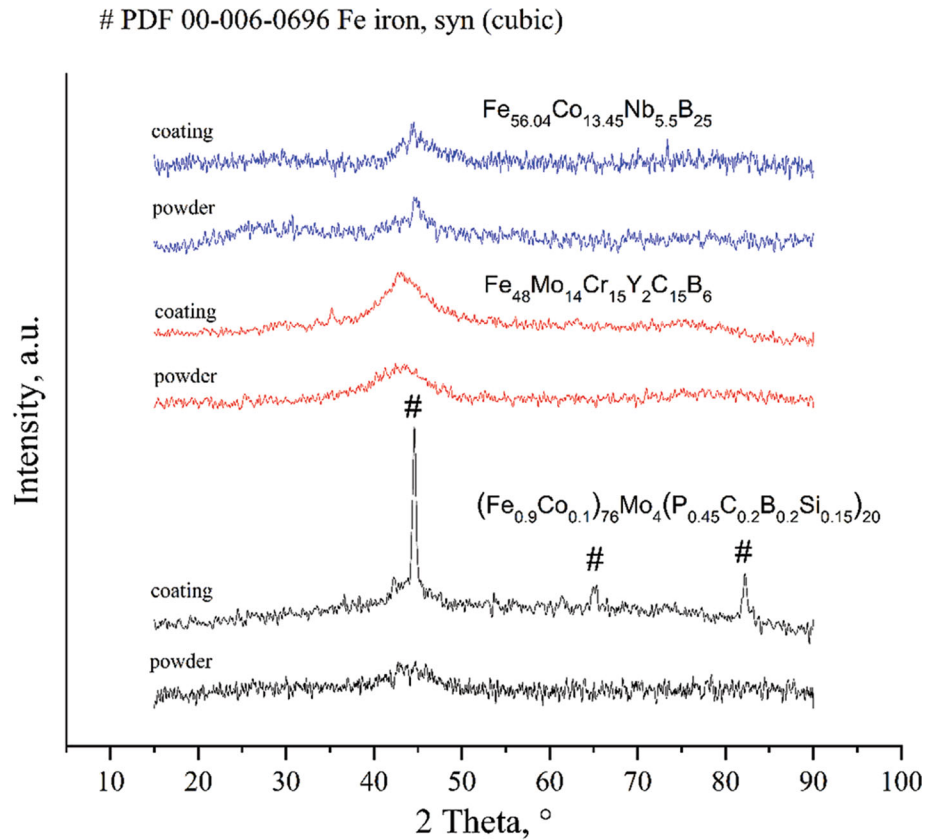**Fig. 4** XRD patterns of the powders and deposited coatings

Fig. 5 (a) Bond strength of deposited coatings, typical fracture: (b) coating, (c) pin

defects in the deposited coatings, e.g., pores, micro-cracks, or crystallites. They are revealed through the use of higher loads and hence a larger area from which data are gathered. The hardness recalculated from nanoindentation for $Fe_{48}Mo_{14}Cr_{15}Y_2C_{15}B_6$ alloy is close to the values obtained for

bulk material (Ref 41). It confirms the amorphous state of the coating. In the case of $Fe_{56.04}Co_{13.45}Nb_{5.5}B_{25}$, the values are much lower than for the bulk material (Ref 26). There is no direct hardness data for $(Fe_{0.9}Co_{0.1})_{76}Mo_4(P_{0.45}C_{0.2}B_{0.2}Si_{0.15})_{20}$, but it can be suspected that the

Table 2. Nanoindentation and hardness measurement results

Parameter Unit	$Fe_{48}Mo_{14}Cr_{15}Y_2C_{15}B_6$				$(Fe_{0.9}Co_{0.1})_{76}Mo_4(P_{0.45}C_{0.2}B_{0.2}Si_{0.15})_{20}$				$Fe_{56.04}Co_{13.45}Nb_{5.5}B_{25}$			
	H_{IT} [MPa]	HV_{IT}	HV0.3	E_{IT} [GPa]	H_{IT} [MPa]	HV_{IT}	HV0.3	E_{IT} [GPa]	H_{IT} [MPa]	HV_{IT}	HV0.3	E_{IT} [GPa]
Mean	12984	1203	1020	173	10882	1008	810	162	10998	1019	792	181
Standard deviation	1144	106	74	9	1048	97	96	9	1430	133	71	8

H_{IT}, indentation hardness; HV_{IT}, Vickers hardness calculated from indentation hardness; $HV_{IT} = H_{IT} / 10.80$, E_{IT}, indentation elastic module

obtained hardness values are lower than for the bulk material. The obtained elastic moduli are also relatively low for iron-based metallic glasses (Ref 42).

Abrasive Wear

The lowest wear was recorded for the $Fe_{48}Mo_{14}Cr_{15}Y_2$-$C_{15}B_6$ coatings (Fig. 6). For coating $Fe_{56.04}Co_{13.45}Nb_{5.5}$-$B_{25,}$ the abrasive wear was twice as high. The highest wear loss was observed for $(Fe_{0.9}Co_{0.1})_{76}$-$Mo_4(P_{0.45}C_{0.2}B_{0.2}Si_{0.15})_{20}$, approximately three times higher than for $Fe_{48}Mo_{14}Cr_{15}Y_2C_{15}B_6$. Overall, the obtained values of $\sim$ 128 mg for $Fe_{48}Mo_{14}Cr_{15}Y_2C_{15}B_6$ and of $\sim$ 242 mg for $Fe_{56.04}Co_{13.45}Nb_{5.5}B_{25}$ appear promising in the background of the literature data (Ref 43). Exemplary, the values given for plasma-sprayed Al_2O coating with a thickness of 200 µm and a porosity of 5% tested under similar conditions amounted to $\sim$ 275 mg after 5 min. In a further step of the test, this coating was destroyed (Ref 43). It must be noted that there is a possibility of further optimization of the coating microstructure toward minimalization of the present defects.

Figure 7 shows the calculated values of η and the H/E ratio from the nanoindentation data. It was observed that wear resistance is not influenced by hardness alone, but elasticity also plays a role. The H/E ratio can be seen as an elastic limit of strain (Ref 44). It indicates the depth that a material can tolerate without exceeding the elastic limit (Ref 45). The η value provides information on how much energy is released after loading the material and is defined as a ratio of the elastic deformation energy to the total deformation energy during the loading-unloading cycle in the nanoindentation test. The total energy might be calculated as the integral of the area under the load depth indentation curve from the start point to the maximum indentation depth. During the unloading phase, materials recover partially, and hence the final indent depth is reduced in comparison to the maximum indentation depth. The elastic energy is given by the integral of the area under the load depth curve from the maximum indentation depth to the final depth. The η value is provided by the following formula:
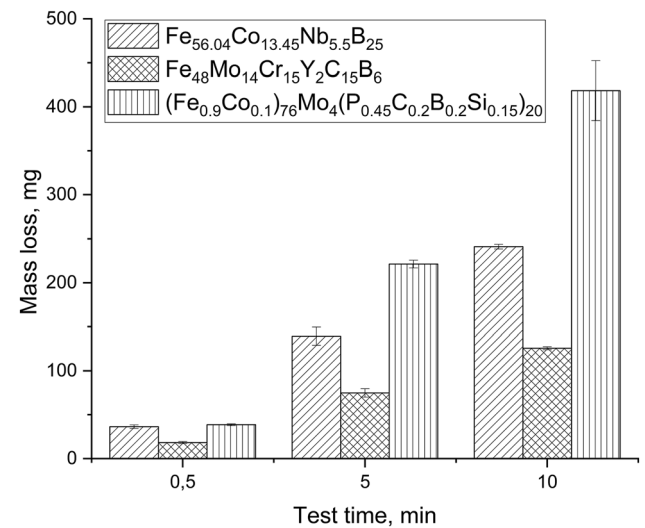

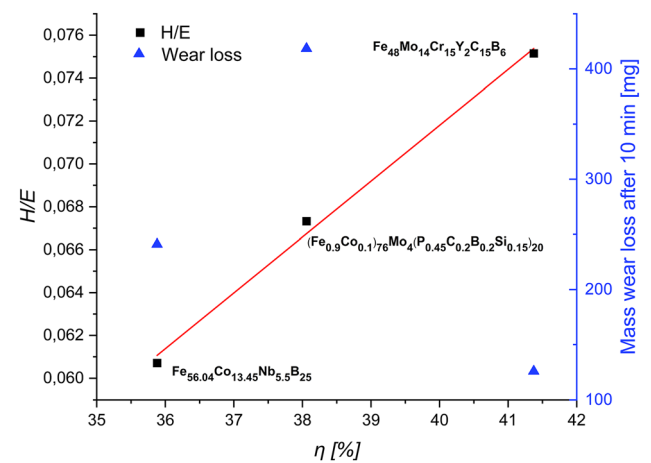**Fig. 6** Rubber wheel test results for deposited coatings

Fig. 7 The relationship between H/E and wear loss for deposited coatings

$$\eta = \frac{E_{\text{elastic}}}{E_{\text{total}}}$$

where: E_{elastic}—elastic deformation energy, E_{total}—total deformation energy.

The higher the η, the greater the material's ability to absorb deformation without damage. Both η and the $H/$
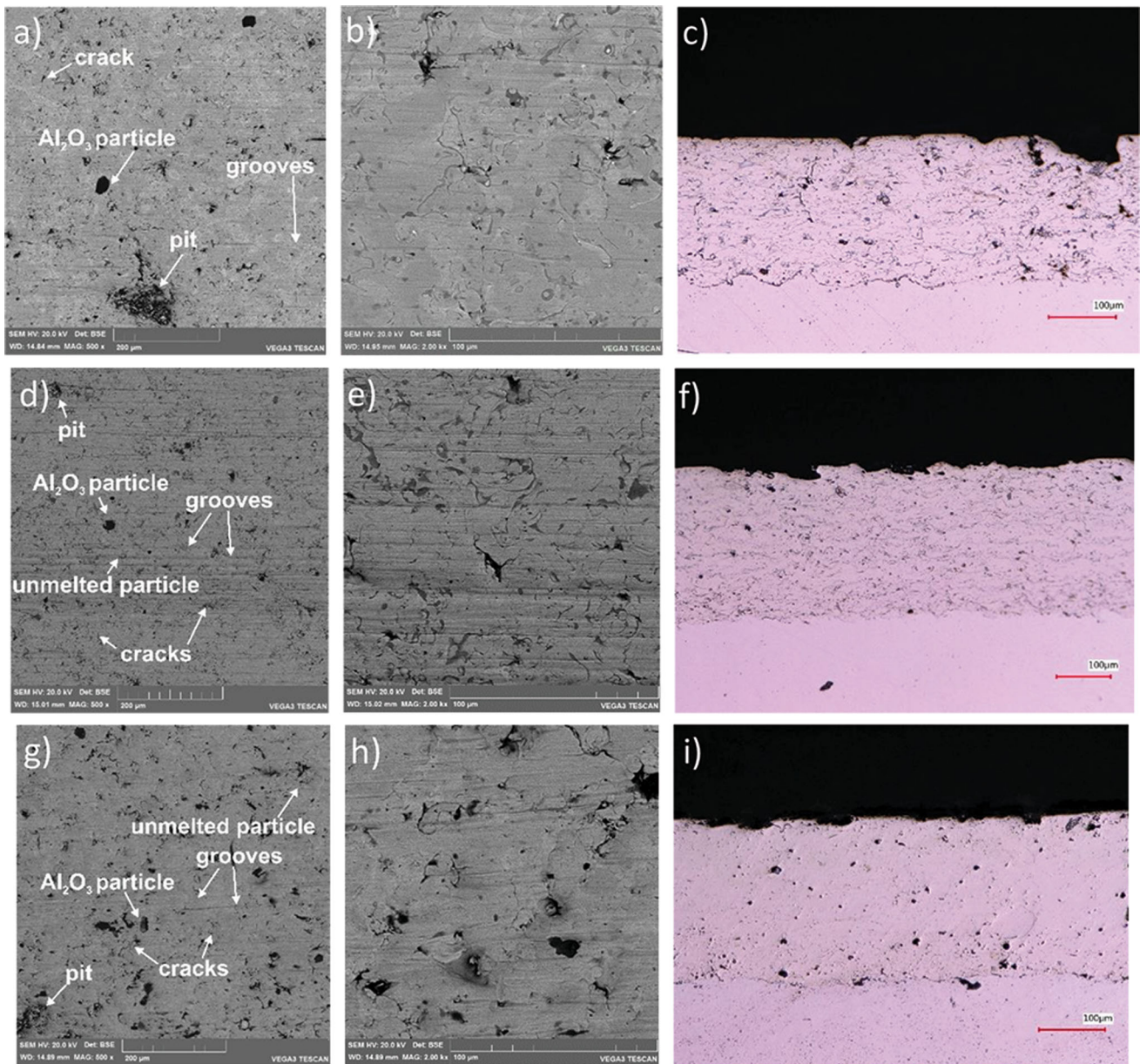
Fig. 8 Coating surfaces and cross sections after abrasive wear test of deposited coatings: (a–c) $Fe_{48}Mo_{14}Cr_{15}Y_2C_{15}B_6$, (d–f) $(Fe_{0.9}Co_{0.1})_{76}$-$Mo_4(P_{0.45}C_{0.2}B_{0.2}Si_{0.15})_{20}$, (g–i) $Fe_{56.04}Co_{13.45}Nb_{5.5}B_{25}$

E ratio can provide information on the resistance to abrasive wear.

The correlation between H/E, η, and the mass wear loss is not perfect. Based on the obtained H/E data, it might be suspected that $Fe_{48}Mo_{14}Cr_{15}Y_2C_{15}B_6$ will have the highest abrasion resistance, followed by $(Fe_{0.9}Co_{0.1})_{76}$-$Mo_4(P_{0.45}C_{0.2}B_{0.2}Si_{0.15})_{20}$ and $Fe_{56.04}Co_{13.45}Nb_{5.5}B_{25}$. However, the mass wear loss for $(Fe_{0.9}Co_{0.1})_{76}$-$Mo_4(P_{0.45}C_{0.2}B_{0.2}Si_{0.15})_{20}$ is unexpectedly high. Figure 8 shows the coatings after the rubber wheel test. The worn surface $(Fe_{0.9}Co_{0.1})_{76}Mo_4(P_{0.45}C_{0.2}B_{0.2}Si_{0.15})_{20}$ coating reveals continuous grooves and some plastic deformation

along the sliding direction. In the other two coatings, with less abrasive wear, grooves are also present, but the surface is smoother. The micro-cutting was partially hindered, and the flacking-off occurred. Micro-cracks might form under abrasion conditions and grow especially at the boundary of the oxide lamella and metallic lamella. After exceeding the critical size, flacking-off occurs (Ref 46). This mechanism is prevailing for brittle materials (Ref 47). It might be observed in the form of pits and micro-cracks for the $Fe_{48}Mo_{14}Cr_{15}$-$Y_2C_{15}B_6$ and $Fe_{56.04}Co_{13.45}Nb_{5.5}B_{25}$ coatings. In the Fe_{48}-$Mo_{14}Cr_{15}Y_2C_{15}B_6$ samples, an additional mechanism was chipping coating fragments due to cracks. The measured

adhesion of the coatings does not allow us to conclude that this results from a lack of cohesion of the entire coating. Instead there are some local lacks of cohesion due, e.g., to cracks or unmelted powder particles. This causes local peeling of the coating fragments, accelerating its abrasive wear. The results obtained show that the best properties were obtained for the coatings with a fully amorphous structure, despite the existing cracks and high brittleness. Interestingly, the $(Fe_{0.9}Co_{0.1})_{76}Mo_4(P_{0.45}C_{0.2}B_{0.2}Si_{0.15})_{20}$ alloy, characterized by the highest plasticity (according to literature 1.7% (Ref 25)), showed the worst properties in the form of coating. The ductility of the $(Fe_{0.9}Co_{0.1})_{76}Mo_4(P_{0.45}C_{0.2}B_{0.2}Si_{0.15})_{20}$ samples was partially confirmed by the low Young's modulus and the abrasive wear mechanism itself. At a hardness comparable to $Fe_{56.04}Co_{13.45}Nb_{5.5}B_{25}$, the coating exhibited much worse wear resistance. One of the reasons may be the oxide content in the $(Fe_{0.9}Co_{0.1})_{76}Mo_4(P_{0.45}C_{0.2}B_{0.2}Si_{0.15})_{20}$ coating which could have significantly affected the hardness results (the $Fe_{56.04}Co_{13.45}Nb_{5.5}B_{25}$ coating was almost not oxidized) and therefore increased the calculated H/E ratio for $(Fe_{0.9}Co_{0.1})_{76}Mo_4(P_{0.45}C_{0.2}B_{0.2}Si_{0.15})_{20}$ coating. Additionally, the presence of the crystallized phase in the form of ferrite in $(Fe_{0.9}Co_{0.1})_{76}Mo_4(P_{0.45}C_{0.2}B_{0.2}Si_{0.15})_{20}$ coating could increase abrasive wear due to its low hardness. It was claimed that the second phase is often introduced into the metallic glass on purpose to increase its toughness (Ref 48). Also, crystallization may improve ductility and reduce abrasive wear (Ref 49). However, this effect was not observed in this study for ferrite precipitates characterized by low hardness.

Conclusions

This study investigated the microstructure and wear properties of three iron-based metal glasses that differ among others in their GFA and plasticity: (1) $Fe_{48}Mo_{14}Cr_{15}Y_2C_{15}B_6$, (2) $(Fe_{0.9}Co_{0.1})_{76}Mo_4(P_{0.45}C_{0.2}B_{0.2}Si_{0.15})_{20}$ and (3) $Fe_{56.04}Co_{13.45}Nb_{5.5}B_{25}$. The powders were produced by gas atomization, and some powder particles contained fine pores due to gas entrapment. The two powders $(Fe_{0.9}Co_{0.1})_{76}Mo_4(P_{0.45}C_{0.2}B_{0.2}Si_{0.15})_{20}$ and $Fe_{56.04}Co_{13.45}Nb_{5.5}B_{25}$ were highly spherical, while the particles of the $Fe_{48}Mo_{14}Cr_{15}Y_2C_{15}B_6$ were slightly elongated, which made feeding more complex and less stable. The powders were used for coating deposition by atmospheric plasma spraying (APS). The coatings were characterized by porosity ranging from 2.8 to 5.3 vol.%. Fully amorphous $Fe_{48}Mo_{14}Cr_{15}Y_2C_{15}B_6$ coatings showed the lowest wear loss despite the vertical crack in their structure. In terms of wear resistance, the second-best performance was obtained with $Fe_{56.04}Co_{13.45}Nb_{5.5}B_{25}$ coatings. The $(Fe_{0.9}Co_{0.1})_{76}Mo_4(P_{0.45}C_{0.2}B_{0.2}Si_{0.15})_{20}$ coating was found to have the lowest wear resistance. The results obtained did not entirely coincide with the calculated values of *H/E*. This could be partially caused by the high oxidation of the $(Fe_{0.9}Co_{0.1})_{76}Mo_4(P_{0.45}C_{0.2}B_{0.2}Si_{0.15})_{20}$ coating and, therefore, the overestimated hardness values compared to the oxide-free and porous $Fe_{56.04}Co_{13.45}Nb_{5.5}B_{25}$ coating. The measured weight loss values were lower than in the case of Al_2O_3 plasma-sprayed coatings, which shows that metallic glasses can be considered promising anti-wear protective materials.

References

1. A. Basu, A.N. Samant, S.P. Harimkar, J.D. Majumdar, I. Manna and N.B. Dahotre, Laser Surface Coating of Fe-Cr-Mo-Y-B-C Bulk Metallic Glass Composition on AISI 4140 Steel, *Surf. Coat. Technol.*, 2008, **202**, p 2623–2631. https://doi.org/10.1016/j.surfcoat.2007.09.028

2. S.K. Nayak, A. Kumar and T. Laha, Developing an Economical Wear and Corrosion Resistant Fe-Based Metallic Glass Composite Coating by Plasma and HVOF Spraying, *J Therm Spray Tech*, 2021 https://doi.org/10.1007/s11666-021-01277-w

3. Y. Huang, Y. Guo, H. Fan and J. Shen, Synthesis of Fe-Cr-Mo-C-B Amorphous Coating with High Corrosion Resistance, *Mater. Lett.*, 2012, **89**, p 229–232. https://doi.org/10.1016/j.matlet.2012.08.114

4. S. Pang, T. Zhang, K. Asami and A. Inoue, Synthesis of Fe-Cr-Mo-C-B-P Bulk Metallic Glasses with High Corrosion Resistance, *Acta Mater.*, 2002, **50**, p 489–497. https://doi.org/10.1016/S1359-6454(01)00366-4

5. M.-W. Tan, E. Akiyama, H. Habazaki, A. Kawashima, K. Asami and K. Hashimoto, The Role of Chromium and Molybdenum in Passivation of Amorphous Fe-Cr-Mo-P-C Alloys in Deaerated 1 M HCl, *Corros. Sci.*, 1996, **38**, p 2137–2151. https://doi.org/10.1016/S0010-938X(96)00071-6

6. B.D. Leonard, F. Sadeghi, S. Shinde and M. Mittelbach, Rough Surface and Damage Mechanics Wear Modeling Using the Combined Finite-Discrete Element Method, *Wear*, 2013, **305**, p 312–321. https://doi.org/10.1016/j.wear.2012.12.034

7. K. Yang, J. Feng, X. Zhou and S. Tao, In-Situ Formed γ-Al_2O_3 Nanocrystals Repaired and Toughened Al_2O_3 Coating Prepared by Plasma Spraying, *Surf. Coat. Technol.*, 2012, **206**, p 3082–3087. https://doi.org/10.1016/j.surfcoat.2011.12.014

8. W. Tian, Y. Wang, Y. Yang and C. Li, Toughening and Strengthening Mechanism of Plasma Sprayed Nanostructured Al_2O_3-13wt.%TiO_2 Coatings, *Surf. Coat. Technol.*, 2009, **204**, p 642–649. https://doi.org/10.1016/j.surfcoat.2009.08.045

9. T. Terajima, F. Takeuchi, K. Nakata, S. Adachi, K. Nakashima and T. Igarashi, Composite Coating Containing WC/12Co

Cermet and Fe-Based Metallic Glass Deposited by High-Velocity Oxygen Fuel Spraying, *J. Alloys Compd.*, 2010, **504**, p S288–S291. https://doi.org/10.1016/j.jallcom.2010.03.209

10. Z. Zhou, L. Wang, D.Y. He, F.C. Wang and Y.B. Liu, Microstructure and Electrochemical Behavior of Fe-Based Amorphous Metallic Coatings Fabricated by Atmospheric Plasma Spraying, *J. Therm. Spray Technol.*, 2011, **20**, p 344–350. https://doi.org/10.1007/s11666-010-9570-4

11. J. Su, J. Kang, W. Yue, G. Ma, Z. Fu, L. Zhu, D. She, H. Wang and C. Wang, Comparison of Tribological Behavior of Fe-Based Metallic Glass Coatings Fabricated by Cold Spraying and High Velocity Air Fuel Spraying, *J. Non-Cryst. Solids*, 2019, **522**, 119582. https://doi.org/10.1016/j.jnoncrysol.2019.119582

12. Y. An, G. Hou, J. Chen, X. Zhao, G. Liu, H. Zhou and J. Chen, Microstructure and Tribological Properties of Iron-Based Metallic Glass Coatings Prepared by Atmospheric Plasma Spraying, *Vacuum*, 2014, **107**, p 132–140. https://doi.org/10.1016/j.vacuum.2014.04.021

13. C. Moreau, P. Cielo, M. Lamontagne, S. Dallaire, J.C. Krapez and M. Vardelle, Temperature Evolution of Plasma-Sprayed Niobium Particles Impacting on a Substrate, *Surf. Coat. Technol.*, 1991, **46**, p 173–187. https://doi.org/10.1016/0257-8972(91)90160-X

14. M. Ashby and A. Greer, Metallic Glasses as Structural Materials, *Scr. Mater.*, 2006, **54**, p 321–326. https://doi.org/10.1016/j.scriptamat.2005.09.051

15. S.F. Guo, J.L. Qiu, P. Yu, S.H. Xie and W. Chen, Fe-Based Bulk Metallic Glasses: Brittle or Ductile?, *Appl. Phys. Lett.*, 2014, **105**, 161901. https://doi.org/10.1063/1.4899124

16. B. Zhang, Q. Dong, N. Zhu, Z. Ba, Y. Han and Z. Wang, Microstructure and Wear Behaviors of Plasma-Sprayed FeCrNi-MoCBSi Coating with Nano-Grain Dispersed Amorphous Phase in Reciprocating Sliding Contact, *Tribol. Trans.*, 2019, **62**, p 274–282. https://doi.org/10.1080/10402004.2018.1547468

17. Z. Chu, W. Deng, X. Zheng, Y. Zhou, C. Zhang, J. Xu and L. Gao, Corrosion Mechanism of Plasma-Sprayed Fe-Based Amorphous Coatings with High Corrosion Resistance, *J. Therm. Spray Technol.*, 2020, **29**, p 1111–1118. https://doi.org/10.1007/s11666-020-01030-9

18. Y. Zhou, G. Ma, H. Wang, G. Li, S. Chen and B. Fu, Microstructures and Tribological Properties of Fe-Based Amorphous Metallic Coatings Deposited via Supersonic Plasma Spraying, *J. Therm. Spray Technol.*, 2017, **26**, p 1257–1267. https://doi.org/10.1007/s11666-017-0582-1

19. M. Wang, Z. Zhou, Q. Wang, L. Wu, Z. Wang and X. Zhang, Long Term Semiconducting and Passive Film Properties of a Novel Dense FeCrMoCBY Amorphous Coating by Atmospheric Plasma Spraying, *Appl. Surf. Sci.*, 2019, **495**, 143600. https://doi.org/10.1016/j.apsusc.2019.143600

20. A. Kumar, S.K. Nayak, P. Bijalwan, M. Dutta, A. Banerjee and T. Laha, Optimization of Mechanical and Corrosion Properties of Plasma Sprayed Low-Chromium Containing Fe-Based Amorphous/Nanocrystalline Composite Coating, *Surf. Coat. Technol.*, 2019, **370**, p 255–268. https://doi.org/10.1016/j.surfcoat.2019.05.010

21. A. Kumar, R. Kumar, P. Bijalwan, M. Dutta, A. Banerjee and T. Laha, Fe-Based Amorphous/Nanocrystalline Composite Coating by Plasma Spraying: Effect of Heat Input on Morphology, Phase Evolution and Mechanical Properties, *J. Alloys Compd.*, 2019, **771**, p 827–837. https://doi.org/10.1016/j.jallcom.2018.09.024

22. P. Bijalwan, A. Kumar, S.K. Nayak, A. Banerjee, M. Dutta and T. Laha, Microstructure and Corrosion Behavior of Fe-Based Amorphous Composite Coatings Developed by Atmospheric Plasma Spraying, *J. Alloys Compd.*, 2019, **796**, p 47–54. https://doi.org/10.1016/j.jallcom.2019.05.046

23. S. Dong, B. Song, X. Zhang, C. Deng, N. Fenineche, B. Hansz, H. Liao and C. Coddet, Fabrication of FeSiB Magnetic Coatings with Improved Saturation Magnetization by Plasma Spray and dry-Ice Blasting, *J. Alloys Compd.*, 2014, **584**, p 254–260. https://doi.org/10.1016/j.jallcom.2013.09.038

24. Z. Zhou, L. Wang, F.C. Wang, H.F. Zhang, Y.B. Liu and S.H. Xu, Formation and Corrosion Behavior of Fe-Based Amorphous Metallic Coatings by HVOF Thermal Spraying, *Surf. Coat. Technol.*, 2009, **204**, p 563–570. https://doi.org/10.1016/j.surfcoat.2009.08.025

25. F. Li, B. Shen, A. Makino and A. Inoue, Excellent Soft-Magnetic Properties of (Fe, Co)-Mo-(P, C, B, Si) Bulk Glassy Alloys with Ductile Deformation Behavior, *Appl. Phys. Lett.*, 2007, **91**, 234101. https://doi.org/10.1063/1.2820608

26. Z.Y. Chang, X.M. Huang, L.Y. Chen, M.Y. Ge, Q.K. Jiang, X.P. Nie and J.Z. Jiang, Catching Fe-Based Bulk Metallic Glass with Combination of High Glass Forming Ability, Ultrahigh Strength and Good Plasticity in Fe-Co-Nb-B System, *Mater. Sci. Eng. A*, 2009, **517**, p 246–248. https://doi.org/10.1016/j.msea.2009.03.082

27. N. Manai, Selective laser melting of SAM1651, an iron-based bulk metallic glass, 2017.

28. J.S. Blázquez, C.F. Conde and A. Conde, Crystallisation Process in (FeCo)78Nb6(BCu)16 Alloys, *J. Non-Cryst. Solids*, 2001, **287**, p 187–192. https://doi.org/10.1016/S0022-3093(01)00562-2

29. I.E. Anderson, E.M. White and R. Dehoff, Feedstock Powder Processing Research Needs for Additive Manufacturing Development, *Curr. Opin. Solid State Mater. Sci.*, 2018, **22**, p 8–15. https://doi.org/10.1016/j.cossms.2018.01.002

30. B.H. Rabin, G.R. Smolik and G.E. Korth, Characterization of Entrapped Gases in Rapidly Solidified Powders, *Mater. Sci. Eng. A*, 1990, **124**, p 1–7. https://doi.org/10.1016/0921-5093(90)90328-Z

31. W.C. Oliver and G.M. Pharr, An Improved Technique for Determining Hardness and Elastic Modulus Using Load and Displacement Sensing Indentation Experiments, *J. Mater. Res.*, 1992, **7**, p 1564–1583. https://doi.org/10.1557/JMR.1992.1564

32. G02 Committee, Test Method for Measuring Abrasion Using the Dry Sand/Rubber Wheel Apparatus, ASTM International, West Conshohocken, PA

33. L. Xie, Y.-M. Wang, X. Xiong and Z.-K. Chen, Comparison of Microstructure and Tribological Properties of Plasma, High Velocity Oxy-Fuel and Detonation Sprayed Coatings from an Iron-Based Powder, *Mater. Trans.*, 2018, **59**, p 1591–1595. https://doi.org/10.2320/matertrans.M2018141

34. C. Minnert, M. Kuhnt, S. Bruns, A. Marshal, K.G. Pradeep, M. Marsilius, E. Bruder and K. Durst, Study on the Embrittlement of Flash Annealed Fe8.52B9.5P4Cu0.8Si0.5 Metallic Glass Ribbons, *Mater. Des.*, 2018, **156**, p 252–261. https://doi.org/10.1016/j.matdes.2018.06.055

35. R. Gerling, F.P. Schimansky and R. Wagner, Two-Stage Embrittlement of Amorphous Fe40Ni40P20 Resulting from A Loss of Free Volume and Phase Separation, *Acta Metall.*, 1988, **36**, p 575–583. https://doi.org/10.1016/0001-6160(88)90090-9

36. F. Li, T. Liu, T. Wang, A. Wang, J. Wang and Y. Yang, Understanding Yielding and the Unusual Ductile-Brittle-Ductile Transition in Fe-Based Amorphous Nanocrystalline Alloy: A Combined Micromechanical and Thermodynamic Study, *J. Mech. Phys. Solids*, 2019, **132**, 103681. https://doi.org/10.1016/j.jmps.2019.103681

37. M. Yasir, C. Zhang, W. Wang, Y. Jia and L. Liu, Enhancement of Impact Resistance of Fe-Based Amorphous Coating by Al_2O_3 Dispersion, *Mater. Lett.*, 2016, **171**, p 112–116. https://doi.org/10.1016/j.matlet.2016.02.060

38. Y. Peng, C. Zhang, H. Zhou and L. Liu, On the Bonding Strength in Thermally Sprayed Fe-Based Amorphous Coatings, *Surf. Coat. Technol.*, 2013, **218**, p 17–22. https://doi.org/10.1016/j.surfcoat.2012.12.018

39. Q. Wang, X. Rui, Q.-J. Wang, Y. Bai, Z.-Z. Du, W.-J. Niu, W. Wang, K.-S. Wang and Y. Gao, Bonding and Wear Behaviors of Supersonic Plasma Sprayed Fe-Based Coatings on Al-Si Alloy

Substrate, *Surf. Coat. Technol.*, 2019, **367**, p 288–301. https://doi.org/10.1016/j.surfcoat.2019.04.003

40. B. Huang, C. Zhang, G. Zhang and H. Liao, Wear and Corrosion Resistant Performance of Thermal-Sprayed Fe-Based Amorphous Coatings: A Review, *Surf. Coat. Technol.*, 2019, **377**, 124896. https://doi.org/10.1016/j.surfcoat.2019.124896

41. J. Shen, Q. Chen, J. Sun, H. Fan and G. Wang, Exceptionally High Glass-Forming Ability of an FeCoCrMoCBY Alloy, *Appl. Phys. Lett.*, 2005, **86**, 151907. https://doi.org/10.1063/1.1897426

42. A. Obeydavi, A. Shafyei, A. Rezaeian, P. Kameli and J.-W. Lee, Fabrication and Properties Evaluation of Novel Fe46-XCr23Mo14Co7PXB5Si5 (X=0, 6) m Metallic Glasses Deposited by DC Magnetron Sputtering, *Intermetallics*, 2021, **131**, 107120. https://doi.org/10.1016/j.intermet.2021.107120

43. T. Lampke, D. Meyer, G. Alisch, D. Nickel, I. Scharf, L. Wagner and U. Raab, Alumina Coatings Obtained by Thermal Spraying and Plasma Anodising—A Comparison, *Surf. Coat. Technol.*, 2011, **206**, p 2012–2016. https://doi.org/10.1016/j.surfcoat.2011.09.006

44. A. Leyland and A. Matthews, On the Significance of the H/E Ratio in Wear Control: A Nanocomposite Coating Approach to Optimised Tribological Behaviour, *Wear*, 2000, **246**, p 1–11. https://doi.org/10.1016/S0043-1648(00)00488-9

45. T.L. Oberle, Properties Influencing Wear Of Metals, *J. Metals*, 1951, **3**, p 438–439.

46. B.-Y. Fu, D.-Y. He, L.-D. Zhao, J.-M. Jiang and X.-Y. Li, Microstructure and Properties of arc Sprayed Coatings Containing Fe Based Amorphous Phase and Nanocrystallites, *Surf. Eng.*, 2009, **25**, p 333–337. https://doi.org/10.1179/026708409X396060

47. J.B. Cheng, X.B. Liang, Z.H. Wang and B.S. Xu, Microstructure and Mechanical Properties of FeBSiNb Metallic Glass Coatings by Twin Wire Arc Spraying, *J. Therm. Spray Technol.*, 2013, **22**, p 471–477. https://doi.org/10.1007/s11666-013-9892-0

48. S. Yoon, J. Kim, B.D. Kim and C. Lee, Tribological Behavior of B4C Reinforced Fe-Base Bulk Metallic Glass Composite Coating, *Surf. Coat. Technol.*, 2010, **205**, p 1962–1968. https://doi.org/10.1016/j.surfcoat.2010.08.078

49. J.B. Cheng, X.B. Liang and B.S. Xu, Devitrification of Arc-Sprayed FeBSiNb Amorphous Coatings: Effects on Wear Resistance and Mechanical Behavior, *Surf. Coat. Technol.*, 2013, **235**, p 720–726. https://doi.org/10.1016/j.surfcoat.2013.08.054